



LaTe_{1.82(1)}: modulated crystal structure and chemical bonding of a chalcogen-deficient rare earth metal polytelluride¹

Hagen Poddig,^a Kati Finzel^b and Thomas Doert^{a*}

Received 7 February 2020

Accepted 10 April 2020

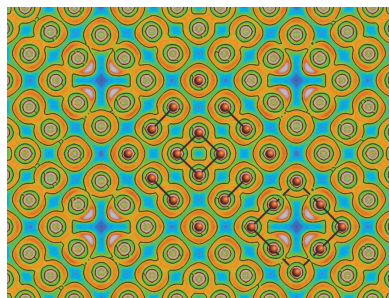
Edited by A. L. Spek, Utrecht University, The Netherlands

¹Dedicated to Professor Stephen Lee on the occasion of his 65th birthday.**Keywords:** modulated structure; rare earth metal polytellurides; bonding analysis; crystal structure; electrical properties.**CCDC references:** 1982148; 1996576**Supporting information:** this article has supporting information at journals.iucr.org/c^aInorganic Chemistry, Technische Universität Dresden, Bergstrasse 66, Dresden 01069, Germany, and ^bTheoretical Chemistry, Technische Universität Dresden, Bergstrasse 66c, Dresden 01069, Germany. *Correspondence e-mail: thomas.doert@tu-dresden.de

Crystals of the rare earth metal polytelluride LaTe_{1.82(1)}, namely, lanthanum telluride (1/1.8), have been grown by molten alkali halide flux reactions and vapour-assisted crystallization with iodine. The two-dimensionally incommensurately modulated crystal structure has been investigated by X-ray diffraction experiments. In contrast to the tetragonal average structure with unit-cell dimensions of $a = 4.4996(5)$ and $c = 9.179(1)$ Å at 296(1) K, which was solved and refined in the space group $P4/nmm$ (No. 129), the satellite reflections are not compatible with a tetragonal symmetry but enforce a symmetry reduction. Possible space groups have been derived by group–subgroup relationships and by consideration of previous reports on similar rare earth metal polychalcogenide structures. Two structural models in the orthorhombic superspace group, *i.e.* $Pmnm(\alpha, \beta, \frac{1}{2})000(-\alpha, \beta, \frac{1}{2})000$ (No. 59.2.51.39) and $Pm2_1n(\alpha, \beta, \frac{1}{2})000(-\alpha, \beta, \frac{1}{2})000$ (No. 31.2.51.35), with modulation wave vectors $q_1 = \alpha a^* + \beta b^* + \frac{1}{2}c^*$ and $q_2 = -\alpha a^* + \beta b^* + \frac{1}{2}c^*$ [$\alpha = 0.272(1)$ and $\beta = 0.314(1)$], have been established and evaluated against each other. The modulation describes the distribution of defects in the planar [Te] layer, coupled to a displacive modulation due to the formation of different Te anions. The bonding situation in the planar [Te] layer and the different Te anion species have been investigated by density functional theory (DFT) methods and an electron localizability indicator (ELI-D)-based bonding analysis on three different approximants. The temperature-dependent electrical resistance revealed a semiconducting behaviour with an estimated band gap of 0.17 eV.

1. Introduction

The structural chemistry of the rare earth metal chalcogenides $REX_{2-\delta}$ ($RE = Y, La-Nd, Sm, Gd-Lu$; $X = S, Se$ or Te ; $0 \leq \delta \leq 0.2$) with trivalent RE metals has attracted attention because of their structural variety in a quite small compositional range. The sulfides and selenides of this class of compounds have been intensively investigated, illuminating several different (super)structures due to different amounts of defects δ and the formation and arrangements of chalcogenide X^{2-} and polychalcogenide X_n^{2-} anions for charge balancing. A comprehensive overview discussing these aspects can be found in Doert & Müller (2016). At the beginning of the 21st century, the structures of four rare earth metal polytellurides $RETe_{2-\delta}$ ($RE = La-Nd$) (Stöwe, 2000*a,b,c*, 2001), were thoroughly (re)investigated, revealing considerable differences to the sulfides and selenides of analogous compositions, while still maintaining the same general structural motif. This general structural motif of all binary polychalcogenides $REX_{2-\delta}$ of trivalent rare earth metals is closely related to the structure of ZrSSi (space group $P4/nmm$, No. 129; $a_0 \simeq 3.80$ and $c_0 \simeq$



OPEN ACCESS

8.00 Å) (Onken *et al.*, 1964; Klein Haneveld & Jellinek, 1964), which shows an alternating stacking of puckered [ZrS] slabs and square-planar [Si] layers along [001]. The binary rare earth metal chalcogenides $REX_{2-\delta}$ ($RE = Y, \text{La-Nd, Sm, Gd-Lu}; X = \text{S, Se or Te}; 0 \leq \delta \leq 0.2$) comprise puckered $[REX]^+$ slabs and planar chalcogenide layers, which can formally be stated as $[X]^-$ (Doert & Müller, 2016). For electronic reasons, the chalcogenide layers of the stoichiometric REX_2 compounds, especially the disulfides RES_2 and diselenides $RESe_2$, feature only X_2^{2-} dianions, resulting in a distortion from an idealized square-planar net towards a planar herringbone pattern; for ditellurides $RETe_2$, the structural situation is not that uniform (Stöwe, 2000*a,b,c*). Going to the off-stoichiometric $REX_{2-\delta}$ ($0 < \delta \leq 0.2$) compounds, vacancies in the planar chalcogenide layers are observed, together with X^{2-} to maintain the overall net charge $[X]^-$ for the layer. This structural change is obvious for the $CeSe_{1.9}$ structure type, but can also be seen for the related, intrinsically disordered Gd_8Se_{15} -type structures (Doert *et al.*, 2012; Doert, Dashjav *et al.*, 2007). Hence, the two most important factors accounting for structural differences are the amount of vacancies in the chalcogenide layer and the ionic radii of the trivalent rare earth metal cations, as they largely determine the Coulomb repulsion between the anions in the $[X]^-$ layers in this series. In addition, in accordance with the Zintl-like electron localization, the polysulfides $RES_{2-\delta}$ and polyselenides $RESe_{2-\delta}$ are semiconductors.

To distinguish between different anionic fragments in the chalcogenide layer, classical electron counting has been proven a simple but powerful way to describe these structures, as briefly explained for the $CeSe_{1.9}$ structure type; the $CeSe_{1.9}$ type is a $\sqrt{5} \times \sqrt{5} \times 2$ superstructure of the basic ZrSSi unit cell and crystallizes in the space group $P4_2/n$ (No. 86) (Plambeck-Fischer *et al.*, 1989). The planar [Se] layer of this compound is built up by four dinuclear Se_2^{2-} anions, forming a pinwheel-like arrangement around a vacancy. The complementary isolated Se^{2-} anion is surrounded by four Se_2^{2-} anions in a spoke-like manner (Lee & Foran, 1994). Assuming only trivalent rare earth metal cations, ten positive charges per $[REX]^+$ layer and unit cell need to be balanced by nine atoms of the planar $[X]^-$ layer. This is achieved by four Se_2^{2-} anions and one isolated Se^{2-} anion. This kind of charge-ordered superstructure has only been reported once for a rare earth metal telluride, namely for $CeTe_{1.9}$ (Ijjaali & Ibers, 2006), whereas many examples are known for the rare earth metal polysulfides and polyselenides (Doert, Graf, Lauxmann *et al.*, 2007; Grupe & Urland, 1991; Plambeck-Fischer *et al.*, 1989; Urland *et al.*, 1989; Dashjav *et al.*, 2000; Müller *et al.*, 2012).

An unusual case of charge balancing for the deficient $REX_{2-\delta}$ compounds has been reported for structures with a composition of $RETe_{1.8}$ (Sm, Gd–Dy) by forming larger anionic fragments (Ijjaali & Ibers, 2006; Wu *et al.*, 2002; Gulay *et al.*, 2007; Poddig *et al.*, 2018). Here, a similar enlargement of the basic lattice parameters of $\sqrt{5} \times \sqrt{5} \times 2$ is observed, and the compounds crystallize in a 10-fold superstructure of the aristotype in $P4/n$ (No. 85). In contrast to the respective sulfides and selenides, a motif of statistically disordered Te_2^{2-}

anions and linear Te_3^{4-} anions are found here. Linear Te_3^{4-} anions have rarely been reported in $REX_{2-\delta}$ compounds, although the presence of an Se_3^{4-} anion was discussed for $DySe_{1.84}$, but neglected after computational studies (van der Lee *et al.*, 1997). The bonding situation in such linear trinuclear anions, like Te_3^{4-} or I_3^- , requires the occupation of nonbonding states, similar to the situation of the prominent XeF_2 molecule. Within the concept of molecular orbital (MO) theory, this situation can be described as a $3c-4e$ bond (Rundle, 1963; Assoud *et al.*, 2007). A density functional theory (DFT)-based study clearly evidenced such a linear Te_3 unit in $GdTe_{1.8}$ (Poddig *et al.*, 2018) and confirmed an alternative method of electron localization for this composition of $REX_{1.8}$: ten positive charges of one puckered $[REX]^+$ layer per unit cell are balanced by two Te_3^{4-} anions and one Te_2^{2-} anion.

Starting from the results of the $RETe_{1.8}$ ($RE = \text{Sm, Gd-Dy}$) compounds, we were interested in identifying the structural motifs of the early rare earth metal tellurides $RETe_{2-\delta}$ with $\delta > 0$. This was especially motivated by the reported differences between the structures of $LaTe_2$, $CeTe_2$ and $PrTe_2$ (Stöwe, 2000*a,b,c*), and the corresponding sulfides and selenides. Structural data on tellurides $RETe_{2-\delta}$ with a comparable low chalcogen content have rarely been reported; $RETe_{1.8}$ ($RE = \text{Sm, Gd-Dy}$) are a few examples (Ijjaali & Ibers, 2006; Wu *et al.*, 2002; Gulay *et al.*, 2007; Poddig *et al.*, 2018). The first results on the lanthanum compound $LaTe_{1.82(1)}$ are presented in the following.

2. Experimental

2.1. Synthesis

All preparation steps were carried out in an argon-filled (5.0, Praxair) glove-box (MBraun, Garching, Germany). Crystals were grown by the addition of a small amount of I_2 to the reaction mixture in closed silica ampoules. In a standard synthesis, 500 mg of a stoichiometric mixture of lanthanum (99.9%, Edelmetall Recycling m&k GmbH) and tellurium (Merck, >99.9%, reduced in a H_2 stream at 673 K) were placed in a quartz tube and flame sealed under dynamic vacuum ($p \leq 1 \times 10^{-3}$ mbar). The ampoule was heated slowly with a ramp of 2 K min^{-1} to 1073 K. The reaction takes place in a gradient from 1123 to 1073 K with I_2 (Roth, >99.8%, purified by sublimating twice prior to use) as transporting agent. After 7 d, the ampoule was cooled to room temperature. As we observed a slow degrading of the compounds under atmospheric conditions, the samples were stored under argon.

2.2. Powder diffraction

Data collection was performed at 296 (1) K with an Emyrean diffractometer (PANalytical) equipped with a curved Ge(111) monochromator using $Cu K\alpha_1$ radiation ($\lambda = 1.54056 \text{ \AA}$). The scans covered the angular range from 5 to $90^\circ 2\theta$. Rietveld refinement using the fundamental parameter approach was performed with *TOPAS* (Version 5; Coelho, 2018).

Table 1
Crystallographic data and refinement details for LaTe_{1.82(1)}.

	Model <i>Pmmn</i>	Model <i>Pm2₁n</i>						
Refined composition	LaTe _{1.811(4)}	LaTe _{1.825(3)}						
Formula weight (g mol ⁻¹); <i>F</i> (000)	370.8; 303	371.8; 304						
Crystal size (mm ⁻³)		0.0588 × 0.0472 × 0.0094						
Diffractometer, radiation		Bruker Kappa APEX II, Mo <i>K</i> α (0.71073 Å)						
Temperature		296 (1) K						
Lattice parameters (Å)		<i>a</i> = 4.5020 (5), <i>b</i> = 4.4985 (5), <i>c</i> = 9.181 (1)						
		$\alpha = \beta = \gamma = 90^\circ$						
Modulation vectors		$q_1 = \alpha a^* + \beta b^* + \gamma c^*$						
		$q_2 = -\alpha a^* + \beta b^* + \gamma c^*$						
		$\alpha = 0.272(1), \beta = 0.314(1), \gamma = \frac{1}{2}$						
Index range measured		$-7 \leq h \leq 8; -8 \leq k \leq 8; -16 \leq l \leq 9; -1 \leq m, n \leq 1$						
		2.18 ≤ θ ≤ 38.36						
Measured reflections		30619						
Absorption coefficient μ (mm)		25.201						
<i>T</i> _{min} ; <i>T</i> _{max}		0.3929, 0.4983						
Extinction parameter (Becker & Coppens, 1974)	0.151	0.153						
Independent reflections	1757, 738 > 3σ(<i>I</i>)	6103, 1386 > 3σ(<i>I</i>)						
Main reflection	415, 323 > 3σ(<i>I</i>)	1080, 719 > 3σ(<i>I</i>)						
First-order satellites	1342, 415 > 3σ(<i>I</i>)	3946, 664 > 3σ(<i>I</i>)						
<i>R</i> _{int} ; <i>R</i> _σ	0.0556, 0.0461 for <i>I</i> > 3σ(<i>I</i>)	0.0469, 0.0600 for <i>I</i> > 3σ(<i>I</i>)						
	0.1563, 0.1934 for all	0.1435, 0.2810 for all						
Superspace group, <i>Z</i>	<i>Pmmn</i> ($\alpha, \beta, \frac{1}{2}$)000(- $\alpha, \beta, \frac{1}{2}$)000 (No. 59.2.51.39), 2	<i>Pm2₁n</i> ($\alpha, \beta, \frac{1}{2}$)000(- $\alpha, \beta, \frac{1}{2}$)000 (No. 31.2.51.35), 2						
Refinement method		JANA2006, full-matrix against <i>F</i> ²						
Restrictions/parameters	0/33	0/66						
	<i>R</i> ₁ [3σ(<i>I</i>)]	<i>R</i> ₁ (all)	<i>wR</i> ₂ [3σ(<i>I</i>)]	<i>wR</i> ₂ (all)	<i>R</i> ₁ [3σ(<i>I</i>)]	<i>R</i> ₁ (all)	<i>wR</i> ₂ [3σ(<i>I</i>)]	<i>wR</i> ₂ (all)
All reflections	0.0495	0.1300	0.0872	0.1111	0.0506	0.2131	0.0883	0.1287
Main reflections	0.0247	0.0385	0.0509	0.0542	0.0326	0.0554	0.0575	0.0610
First-order satellites	0.1079	0.2470	0.1891	0.2479	0.1000	0.3333	0.1949	0.2928
Goodness-of-fit [3σ(<i>I</i>)/all]	1.53/1.26	1.30/0.90						
Largest difference peak/hole (e Å ⁻³)	15.11/-17.25	13.21/-14.87						

Computer programs: APEX2 (Bruker, 2010), SAINT-Plus (Bruker, 2017), SHELXT2014 (Sheldrick, 2015a), SUPERFLIP (Palatinus & Chapuis, 2007), SHELXL2019 (Sheldrick, 2015b), JANA2006 (Petříček *et al.*, 2014), OLEX2 (Dolomanov *et al.*, 2009), SADABS (Krause *et al.*, 2015) and DIAMOND (Brandenburg, 2019).

2.3. Single-crystal diffraction

Crystal data, data collection and structure refinement details are summarized in Table 1. Data for the modulated structure were integrated and corrected for Lorentz and polarization factors, before applying a numerical absorption correction with the program JANA2006 (Petříček *et al.*, 2014).

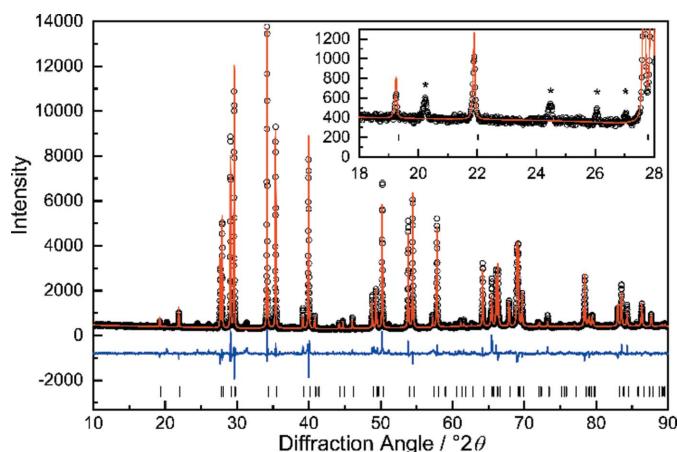


Figure 1
Rietveld refinement of LaTe_{1.82(1)}. The space group of the aristotype ZrSi (*P4/nmm*), with corresponding atom sites as the starting point for structure analyses, has been chosen. Satellite reflections are marked with an asterisk.

The structure was solved using the charge-flipping method of the program SUPERFLIP (Palatinus & Chapuis, 2007) implemented in the JANA2006 software; the atomic positions were synchronized with those of the average structure. Structure refinement was performed with JANA2006 against *F*² including anisotropic displacement parameters for all atoms. Second-order satellites were neglected because of their low intensity (about 99% of these reflections were found with intensities below 3σ) and two harmonic waves have been used for the fit of the atomic modulation functions.

2.4. Scanning electron microscopy (SEM) and EDS

SEM was performed with an SU8020 (Hitachi) with a triple-detector system for secondary and low-energy backscattered electrons (*U*_a = 5 kV). The composition of selected single crystals was determined by semiquantitative energy dispersive X-ray analysis (*U*_a = 20 kV) with a Silicon Drift Detector (SDD) X-Max^N (Oxford).

2.5. Computational methods

Solid-state calculations were performed with the all-electron code FHI-aims (Blum *et al.*, 2009) for three ordered structural models of LaTe_{1.82(1)}. The FHI-aims calculations for subsequent real-space analysis were performed with a (2 × 2 × 2) *k*-point grid (model in *P1*) and a (3 × 2 × 2) *k*-point grid

(model in *Amm2* and *A2*) using the zeroth-order scalar relativistic zora correction, collinear spins, the numerical atom-centred basis of light level and the PBE functional (Perdew *et al.*, 1996). Real-space properties were evaluated subsequently with the help of the program package *DGrid* (Kohout, 2016). Hereby, the electron localizability indicator (ELI-D) was calculated on a grid with a 0.1 Bohr mesh size.

2.6. Temperature-dependent electrical resistance

The electrical resistance of $\text{LaTe}_{1.82(1)}$ was measured between 7 and 345 K with a mini-CFMS (Cryogenic Ltd, London). Four gold contacts were attached to the surface of a single crystal in a linear set-up with a carbon conductive composite 7105 (DuPont) to establish the electrical contact between the crystal and the gold wires.

3. Results and discussion

3.1. Synthesis

Black plate-like single crystals of previously unreported $\text{LaTe}_{1.82(1)}$ were obtained starting from the elements by alkali halide flux reactions or solid-state reactions with a small amount of I_2 for mineralization in fused-silica ampoules. Temperatures above 1173 K in the presence of I_2 lead to an attack on the ampoule wall, whereas temperatures of about 1073 to 1123 K are well suited for crystal growth, without noticeable side reactions with the ampoule material. The best results were achieved in a small gradient from 1123 to 1073 K, where crystals of about 0.3 mm in length were grown. The amount of added I_2 needs to be compensated by excess La when preparing the experiment due to the formation of LaI_3 during and after the experiment, which in turn alters the composition slightly. Solid LaI_3 was mainly found at the sink of the ampoule, whereas the desired product was found at the source of the ampoule. A similar procedure at higher temperatures was chosen, *e.g.* for $\text{RETe}_{1.8}$ ($\text{RE} = \text{Gd}, \text{Tb}$ or Dy) (Poddig *et al.*, 2018).

3.2. Diffraction image

The strong reflections of the powder pattern can be indexed with a tetragonal unit cell with $a = b \simeq 4.50 \text{ \AA}$ and $c \simeq 9.17 \text{ \AA}$. As a starting point for the Rietveld refinement, the space group ($P4/nmm$, No. 129) and the atom sites of the aristotype, the ZrSSi type, were chosen. The fit shows some additional unindexed reflections, which are not compatible with the space group $P4/nmm$ and its most prominent lower symmetric subgroups (Fig. 1).

The diffraction image of a single crystal at ambient temperature reveals, as already indicated by powder diffraction, additional weak reflections in the layers (hkn) with $n = 0, \pm 1, \pm 2, \dots$ (Fig. S1 in the supporting information). Slightly stronger reflections can be observed in the layers (hkn) with $n = \pm 0.5, \pm 1.5, \dots$ (Fig. S1). These additional reflections cannot be indexed with a commensurate superstructure of the basic unit cell and were treated as satellites. Moreover, the distribution of the satellites with respect to the main reflec-

tions suggest a two-dimensional modulation. The whole diffraction image can then be indexed with five indices $hklm_1m_2$ according to:

$$H_i = ha^* + kb^* + lc^* + m_1q_1 + m_2q_2$$

with

$$q_1 = \alpha a^* + \beta b^* + \frac{1}{2}c^*$$

and

$$q_2 = -\alpha a^* + \beta b^* + \frac{1}{2}c^*.$$

The modulation wave vector components α and β were determined to be 0.272 (1) and 0.314 (1), respectively. A schematic image of the relative positions of the satellite reflections with respect to the main reflections is displayed in Fig. 2 and reconstructed precession images are shown in Fig. S1 (see supporting information). The schematic figure illustrates also that two different q vectors are necessary to index the complete diffraction image. Equivalent satellites are linked by a twofold rotational axis (Fig. S1), pointing towards orthorhombic (or lower) symmetry for the modulated structure. Furthermore, the weak additional reflections in the (hkn) ($n = \pm 1, \pm 2, \dots$) plane correspond to the linear combinations of q_1 and q_2 , which cannot be explained by twinning and are, thus, evidencing a true $[3 + 2]$ -dimensional modulated structure.

3.3. Average crystal structure

Single-crystal data collected at ambient temperature indicated the same lattice parameters for a and b within standard deviations so that a tetragonal unit cell of $a = 4.4996$ (5) and $c = 9.179$ (1) \AA was chosen. The main reflections are clearly compatible with high tetragonal Laue symmetry and the space group $P4/nmm$ (No. 129) was chosen for structure refinement of the average structure according to the reflection condition $h+k = 2n$. The refinement resulted in a reasonable structural model (Table S1 in the supporting information), with a reduced occupancy factor of the Te site in the Te layer of about 81.1 (4)%. The composition derived from semiquantitative

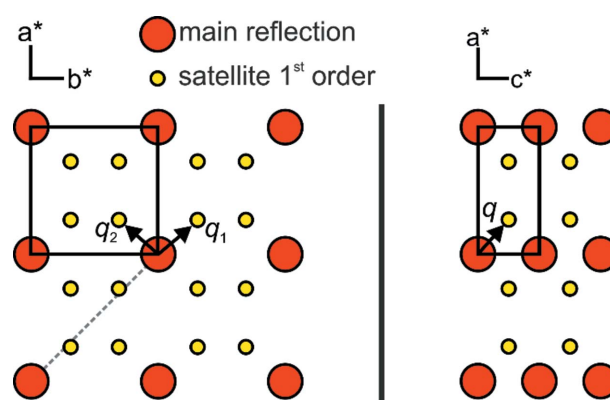


Figure 2
Projection of the relative position of the main reflections and first-order satellites along the [001] (left) and [010] (right) directions. The dotted line indicates the deviation of the satellite positions from the [110] mirror plane in Laue class $4/mmm$.

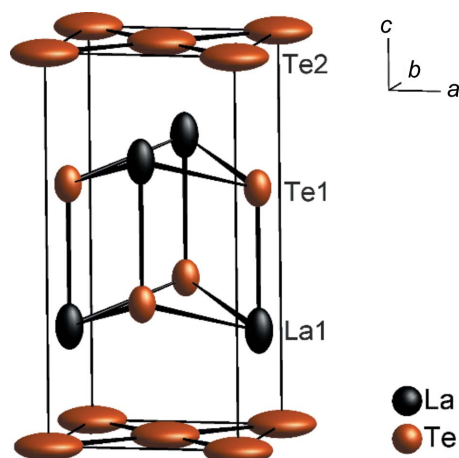


Figure 3
Average crystal structure of $\text{LaTe}_{1.82(1)}$. Displacement ellipsoids are drawn with a probability level of 99.9%.

EDS (energy-dispersive X-ray spectroscopy) measurements points towards a composition of $\text{LaTe}_{1.79(1)}$. Throughout the article, we will refer to this compound as $\text{LaTe}_{1.82(1)}$, based on the refined composition of the modulated structure.

The average structure of $\text{LaTe}_{1.82(1)}$ can be described with puckered [LaTe] layers sandwiched by square-planar [Te] layers. The partial occupation of the Te position in the [Te] layer, together with its large oblate anisotropic displacement parameters (ADPs) in the ab plane and prolate ADPs of the La atom along the [001] direction already give hints towards the modulation (Fig. 3).

The La atoms are regularly surrounded by five Te atoms of the puckered layer [$4 \times 3.3006(4)$ and $1 \times 3.324(1) \text{ \AA}$] and four Te atoms of the [Te] layer [$4 \times 3.3563(7) \text{ \AA}$], forming a regular tricapped trigonal prism. The planar [Te] layer is a perfect square net of Te atoms, with a Te–Te distance of $3.1821(4) \text{ \AA}$, which is significantly longer than a single Te–Te bond with about 2.80 \AA [e.g. 2.78 \AA in Rb_2Te_2 , 2.86 \AA in $\alpha\text{-K}_2\text{Te}_2$ or $2.790(1) \text{ \AA}$ in $\beta\text{-K}_2\text{Te}_2$; Böttcher *et al.*, 1993]. The large ADPs indicate a considerably reduced electron density and a positional shift of the Te atoms due to the formation of anionic Te units. Similar observations have been made for the incommensurable modulated selenides $\text{RESe}_{1.85}$ ($\text{RE} = \text{La-Nd}$ or Sm) (Doert, Graf, Schmidt *et al.*, 2007; Graf & Doert, 2009).

3.4. Refinement of the modulated structure

The tetragonal symmetry of the average structure discussed above is violated by the modulation vectors, as mentioned before. The observed satellite positions are incompatible with a fourfold rotational axis (Fig. 2), resulting in a lower symmetric Laue class. To establish a suitable basic structure as starting model, orthorhombic and monoclinic subgroups of the space groups of the average structure were considered. The highest possible orthorhombic space group would then be $Pm\bar{m}n$, which is a *translationengleiche* subgroup of the index 2 (t_2) of $P4/nmm$, as displayed in Fig. 4. However, a very similar basic structure has been used for $\text{DySe}_{1.84}$, with similar modulation wave vectors $q_1 = \alpha a^* + \beta b^* + \frac{1}{2}c^*$ and $q_2 = \alpha a^* -$

$\beta b^* + \frac{1}{2}c^*$, with $\alpha = 0.333$ and $\beta = 0.273$. The structure model obtained in superspace group $Pm\bar{m}n(\alpha, \beta, \frac{1}{2})000(\alpha, -\beta, \frac{1}{2})000$ [No. 59.2.51.39 according to Stokes *et al.* (2011)] contained linear Se_3^{4-} units besides Se_2^{2-} and Se^{2-} anions. The existence of linear Se_3^{4-} fragments, however, was excluded due to energetic consideration based on the μ_2 -Hückel method (van der Lee *et al.*, 1997) and the final model for $\text{DySe}_{1.84}$ was established in the noncentrosymmetric space group $Pm2_1n(\alpha, \beta, \frac{1}{2})000(\alpha, -\beta, \frac{1}{2})000$ (No. 31.2.51.35). We therefore decided to establish a second structure model for $\text{LaTe}_{1.82(1)}$ in $Pm2_1n(\alpha, \beta, \frac{1}{2})000(-\alpha, \beta, \frac{1}{2})000$, too, and evaluate it against the centrosymmetric one in $Pm\bar{m}n(\alpha, \beta, \frac{1}{2})000(-\alpha, \beta, \frac{1}{2})000$. The group–subgroup relationship between these two space groups of the basic structures is displayed in Fig. 4, indicating a t_2 group–subgroup relationship between them. The limits of both models shall be discussed in the following and the crystallographic details of the refinements are given in Table 1.

The main reflections meet the conditions for a primitive tetragonal lattice nearly perfectly, the data derived by powder diffraction and single-crystal diffraction give no hint of an orthorhombic or even monoclinic distortion of the lattice within standard uncertainties. However, taking the symmetry of the satellite reflections into account, the final unit-cell parameters were restrained to the conditions of an orthorhombic unit cell and were used for the integration of the intensities, as well as for structure refinements. According to the two modulation vectors and reflection conditions, the proper superspace group is $Pm\bar{m}n(\alpha, \beta, \frac{1}{2})000(-\alpha, \beta, \frac{1}{2})000$ (No. 59.2.51.39). The modulated structure clearly contradicts twinning: the result of a fourfold rotational axis as twin element would result in four additional satellite reflections

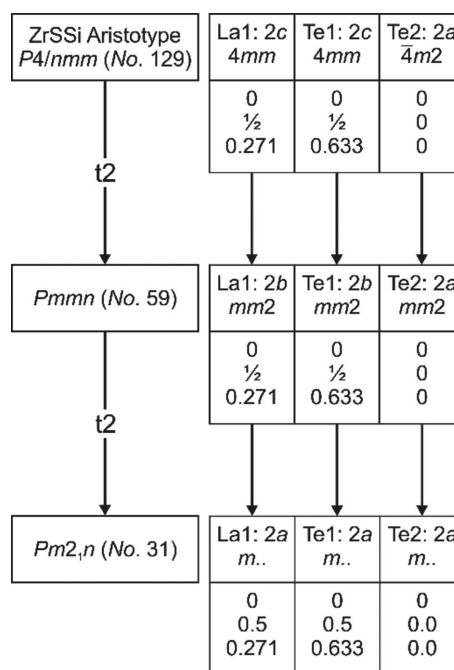


Figure 4
Group–subgroup relationship between the space group of the aristotype ZrSSi ($P4/nmm$) and the chosen orthorhombic space groups of the basic structures.

around the position of the main reflections in layers hkl , $l = \pm 0.5, \pm 1.5, \dots$ (Fig. S2 in the supporting information). The reconstructed precession images, however, reveal only the four expected satellite reflections corresponding to $\pm q_1$ and $\pm q_2$.

A second model in superspace group $Pm2_1n(\alpha, \beta, \frac{1}{2})-000(-\alpha, \beta, \frac{1}{2})000$ (No. 31.2.51.35; we keep the nonstandard setting for a concise structure description) has been evaluated against the centrosymmetric model to check if there are also differences in the structural model, as in the case of $\text{DySe}_{1.84}$. For simplicity, we will use the three-dimensional space-group symbols during the structure descriptions to distinguish between the two different modulated structures in the following.

The refinement in $Pm2_1n$ has been adjusted by considering inversion twinning. The refinement converged with a twin volume fraction of about 40% for the second domain.

The atomic modulation functions (*amf*) were stepwise included in both refinements, by first modelling the positional displacement of all atoms, before including an additional occupational modulation for the Te2 atom. As already expected from the average structure, the La1 and Te1 position show mainly shifts in the c direction, whereas the Te2 atom in the [Te] layer shows a strong displacement in the ab plane, as displayed in the two t plots in Fig. 5. Note, that there is a small difference for the positional modulation along [001] for the Te2 atom between the models in $Pm\bar{m}n$ and $Pm2_1n$, as a result of the higher degree of freedom in the noncentrosymmetric

space group. In $Pm2_1n$, the t plot shows a slightly sinusoidal curve in the c direction with a very small amplitude.

The displacement in the [LaTe] layer along c can be explained as a reaction to the modulation in the [Te] layer; the La atom aims to compensate the missing Te atoms in the coordination sphere by getting closer to the [Te] layer. Consequently, the Te1 atom reacts accordingly to the La1 dislocation by adjusting its position along c as well. The displacement of the Te2 atom in the [Te] layer is slightly more pronounced (Fig. 5), due to vacancy formation and the creation of different Te anions. This holds for both models, as mentioned before. As a second step in the refinement, the occupational modulation in the [Te] layer was introduced by adding two harmonic functions. This improved the structural model in $Pm\bar{m}n$ and $Pm2_1n$ considerably and the areas of low electron density at certain points in the Fourier map around Te2 are now also covered by the atomic modulation function (Fig. 6).

The Fourier sections in Fig. 6 also reveal a partially discontinuous behaviour of the electron density around Te2, although it is not very pronounced (see also Fig. S3 in the supporting information for a two-dimensional plot of the Te occupancy). The drawback in modelling this with harmonic functions are some overshooting and truncation effects in the final structure model, which we assume to be one major reason for the large residual electron-density maxima (see Table 1). The interatomic distances are, nevertheless, in good agreement with previously reported distances for Te anions and the refined composition matches that of the semiquantitative EDS analysis. In the second evaluated model in $Pm2_1n$, harmonic functions, as well as crenel functions, have been utilized. The refinement with harmonic waves in $Pm2_1n$ converged with slightly better R values and a similar residual electron density compared to the refinement in $Pm\bar{m}n$, mainly due to the greater number of independently refined parameters. The use of discontinuous functions, such as crenel or sawtooth functions (Petříček *et al.*, 2016), failed in $Pm\bar{m}n$ but refined stably in $Pm2_1n$, although they did not improve the structural model. The comparison between both types of functions suggests that treating the occupational and positional modulation of Te2 by harmonic functions is suitable. The large residual peaks in the difference Fourier ($F_o - F_c$) maps decrease considerably if two modulation functions are applied to the ADPs of Te2 as well. However, this leads to nonpositive-definite values for U_{\min} at some values of t and has hence been rejected for the final structure model.

3.5. Discussion of the modulated crystal structure of $\text{LaTe}_{1.82(1)}$

The structure model derived in $Pm\bar{m}n(\alpha, \beta, \frac{1}{2})000(-\alpha, \beta, \frac{1}{2})000$ for $\text{LaTe}_{1.82(1)}$ is used in the following paragraph for the discussion of the structural features as the structural differences between both models are negligible, as stated before.

The general feature of an alternating stacking of a puckered [LaTe] layer and [Te] layer is easily seen from Fig. S4 (see supporting information), which additionally shows the

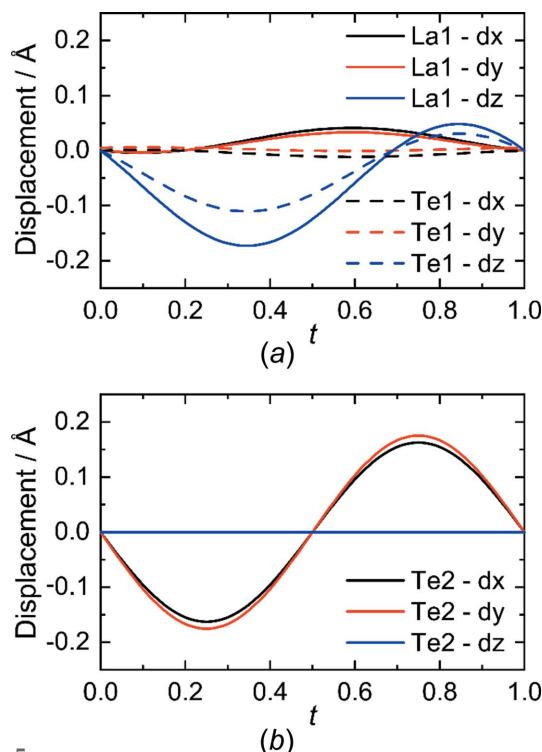


Figure 5
 t -plots (a) of the displacement of La1 and Te1 in the [LaTe] layer and (b) of Te2 in the [Te] layer.

displacement of the La atoms along the c direction, as expected from the average structure. The motif of the puckered layer is very stable and does not show large deviations between different $REX_{2-\delta}$ compounds, whereas the planar $[X]$ layer is the more interesting structural feature and will be discussed in the following.

The change of the occupation and the variations of the Te–Te distances for the model in $Pmmn$ are shown in Fig. 7. The t -plot for the occupational modulation displays a static behaviour along t , which is shifted for different u values. The changes of the Te–Te distances in the modulated $[Te]$ layer are displayed in the second t plot (Fig. 7). Short distances with a lower limit of 2.801 (4) Å correspond to a Te–Te single bond (see above) and medium distances up to 2.959 (1) Å are in good agreement with distances reported for a linear Te_3^{4-} anion (see, for example: Poddig *et al.*, 2018), as well as the often observed Te_2^{2-} anions (see, for example: Stöwe, 2000a). Larger distances of 2.984 (1) to 3.563 (4) Å are mainly considered as nonbonding interactions between Te entities. Compared to the known rare earth metal polysulfides and selenides, the interpretation of the Te–Te distances from a purely crystallographic viewpoint is more difficult as we face a much larger variety of distances, and boundaries between bonding and nonbonding interactions in the $RETe_{2-\delta}$ system are floating. Reported Te–Te distances in dinuclear Te_2^{2-} anions ranging from 2.868 (1) Å in $GdTe_{1.8}$ (Poddig *et al.*, 2018) to 3.036 (2) Å in $LaTe_2$ (Stöwe, 2000a) have been interpreted as single bonds. Nevertheless, the observed distances in the modulated structure of $LaTe_{1.82(1)}$ are in good agreement with the distances found in comparable compounds.

A section of the modulated $[Te]$ layer is depicted in Fig. 8, with Te positions displayed for a refined occupancy factor of 0.5 and greater. Solid lines indicate distances from 2.801 (4) up to 2.981 (2) Å, which should illustrate probable bonding situations; dashed lines are drawn up to 3.282 (2) Å for a

better visualization of possible larger fragments, which have been reported for other polychalcogenides. Considering only these distances, three different motifs can be distinguished: a Te_8 unit, probably consisting of smaller anions, like Te^{2-} , Te_2^{2-} , bent Te_3^{2-} and linear Te_3^{4-} anions, as well as isolated Te^{2-} anions surrounded by different anionic Te entities. Eight-membered rings of chalcogen atoms and isolated X^{2-} anions are, as already pointed out, common motifs in the crystal structures of the rare earth metal sulfides and selenides with compositions of $RES_{1.9}$ ($RE = La-Nd, Sm, Gd-Tm$) (Doert, Graf, Lauxmann *et al.*, 2007; Tamazyán *et al.*, 2000; Müller *et al.*, 2012), $RESe_{1.9}$ ($RE = La-Nd, Sm, Gd-Tm$) (Grupe & Urland, 1991; Plambeck-Fischer *et al.*, 1989; Urland *et al.*, 1989; Müller *et al.*, 2012), $RE_8S_{15-\delta}$ ($RE = Y, Tb-Ho$) (Doert *et al.*, 2012), $RE_8Se_{15-\delta}$ ($RE = Y, Gd-Er; \delta = 0 \leq \delta \leq 0.3$) (Doert, Dashjav *et al.*, 2007) and $RESe_{1.85}$ ($RE = La-Nd$ or Sm) (Doert, Graf, Schmidt *et al.*, 2007; Graf & Doert, 2009).

In the modulated $[Te]$ layer of $LaTe_{1.82(1)}$, a Te_4 square is apparent additionally when choosing small cut-off values for the approximant crystal structure for visualization (see, for example: Fig. S5 in the supporting information). As all four atoms in these fragments have an occupation value of about 0.52 (5), the presence of all four at the same time seems unrealistic. Instead, an unresolved superposition of a dinuclear Te_2^{2-} anion with two adjacent vacancies is the most likely explanation. Moreover, there is no evidence for anionic $[Te_4]$ squares with Te–Te distances of 2.80 Å in the literature. Cationic Te_4^{2+} and the corresponding Se_4^{2+} entities, on the other hand, are well known (see, for example: Barr *et al.*, 1968; Beck *et al.*, 1997; Forge & Beck, 2018; Ruck & Locherer, 2015) and their bonding situation has been investigated by computational methods in 1980 already (Rothman *et al.*, 1980). The typical Te–Te distance in Te_4^{2+} is about 2.65 to 2.70 Å (Ruck & Locherer, 2015) and the Te–Te–Te angles are often close to 90°, which results in a slight distortion from idealized D_{4h} symmetry. Taking the EDS results and the site-occupation

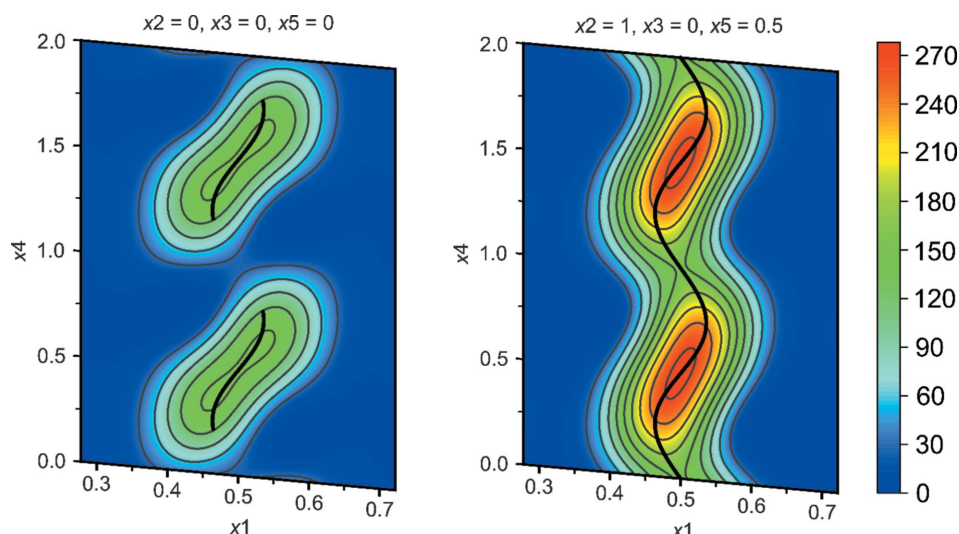


Figure 6

Fourier sections around Te_2 . The electron density is drawn in contour line steps of 30 \AA^{-3} . The central thick black line indicates the refined modulation function.

factor from the average structure (both resulting in a composition of about $\text{LaTe}_{1.8}$) into account, a substantial number of voids in the [Te] layer is expected, which also supports the idea of a disordered motif of dinuclear Te_2^{2-} anions and adjacent vacancies instead.

A similar discussion of apparent structure motifs and possible (super)positions due to unresolved disorder shall be deduced for the apparent Te_8 rings (Fig. 8). Arrangements of disordered X_2^{2-} anions have been identified as the constituents of eight-membered ring-like motifs in the sulfides $RE_8S_{15-\delta}$ ($RE = \text{Y, Tb-Ho}$; Doert *et al.*, 2012) and selenides $RE_8Se_{15-\delta}$ ($RE = \text{Y, Gd-Er}$; $\delta = 0 \leq \delta \leq 0.3$; Doert, Dashjav *et al.*, 2007). In $\text{LaTe}_{1.82(1)}$, these apparent eight-membered rings may also consist of different disordered constituents, like Te_3^{2-} and Te_3^{4-} anions, along with the more common Te_2^{2-} and Te_2^{2-} motifs, around central vacancies. However, this is hard to resolve solely from the diffraction data. To gain more insight into this structural motif and the chemical bonding situation in the modulated [Te] layers in general, chemical bonding analyses were performed for three different commensurate approximants.

3.6. Bonding analysis

Quantum mechanical calculations based on density functional theory (DFT) and bonding analyses with the electron localizability indicator (ELI-D) (Kohout, 2004, 2006; Pendás *et al.*, 2012) have been performed for three approximant structures of $\text{LaTe}_{1.82(1)}$ in order to provide additional information on the bonding situation in the Te layers, especially regarding the (presumably disordered) Te_4 and Te_8 entities. As these

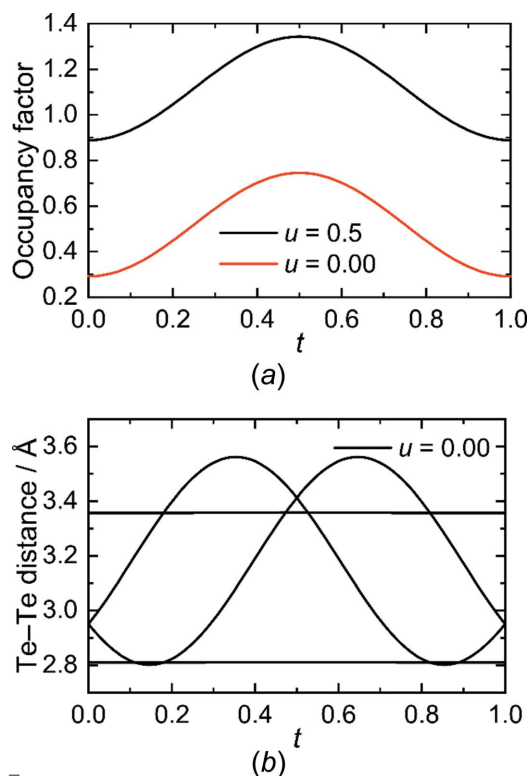


Figure 7
 t -plots of (a) the occupation and (b) the distances shown for $\text{LaTe}_{1.82(1)}$.

calculations require three-dimensional commensurate structure models as bases, a suitable commensurate orthorhombic B -centred $4 \times 3 \times 2$ supercell of the basic ZrSSi -type structure was chosen by approximating the q vector components α and β by $\frac{1}{4}$ and $\frac{1}{3}$, respectively. The respective three-dimensional space groups and the atomic positions were derived by the *JANA2006* software package (Petříček *et al.*, 2014) by enabling the commensurate option, after the final refinement of the modulated structure. According to the previously reported structures of $RESe_{1.875-\delta}$ compounds (Doert, Dashjav *et al.*, 2007; Stöwe, 2001), this cell was transformed into an A -centred setting for a better comparison, resulting in a $3 \times 4 \times 2$ supercell with unit-cell dimensions of $a = 13.4859$ (4), $b = 17.9812$ (4) and $c = 18.3446$ (8) Å. As the highest possible symmetry, space group $Amm2$ (No. 38), the space group of the $RE_8Se_{15-\delta}$ compounds, was chosen for one approximant. The respective $Amm2$ structure model exhibits bent Te_3 units in the Te_8 ring, as well as a Te_4 square, which cannot be resolved due to the symmetry restrictions in this space group (Fig. S6 in the supporting information). A second model has been established in the space group $A2$ (No. 5), *i.e.* removing the two perpendicular mirror planes. This space group has also been used to describe the disorder in the structures of the compounds $RE_8S_{15-\delta}$. Here, only Te_2^{2-} anions with alternating short (bonding) and longer (nonbonding) distances are considered as building units of the Te_8 rings (Fig. S7 in the supporting information), enabling a direct comparison between the bent X_3 fragments in $Amm2$, and the X_2^{2-} patterns known from different $REX_{1.9}$ and $RE_8X_{15-\delta}$ structures (*cf.* above). A third model in the space group $P1$ (No. 1) was developed starting from the previous model in $A2$ to lift the symmetry restrictions completely. The disorder of the apparent Te_4 unit can then be resolved by assuming two

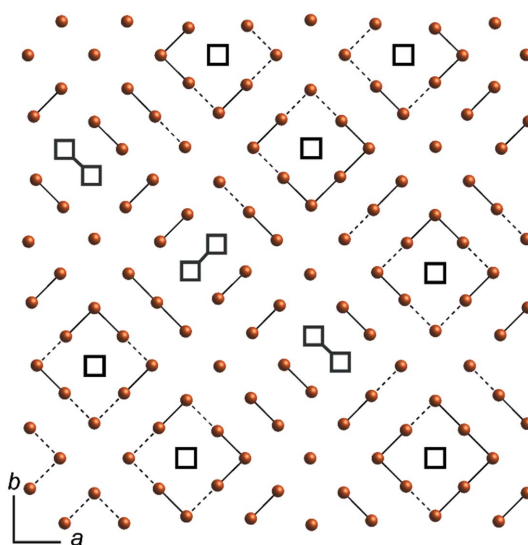


Figure 8
Section of the modulated Te layer, with a cut-off occupancy at 0.5. Black-framed squares emphasize the voids in the layer. Solid lines are drawn from 2.801 to 2.981 Å and dashed lines are drawn for distances between 2.984 to 3.282 Å.

vacancies and a single Te_2^{2-} anion (Fig. S8 in the supporting information). Bear in mind that energetic comparisons are only possible between models with the same number of atoms. This is the case for the models in *Amm2* and *A2*, but not for *P1*, due to the additional vacancies when taking the occupational disorder of the Te_4 square into account. This means that an identification of the favoured structure is not possible based on the computed net energies only.

The calculated band gaps for all models are finite, but small, e.g. 0.04 eV for the model in *A2*, so that semiconducting electronic properties are expected (see below). The corresponding stoichiometric LaTe_2 was reported as metallic (Stöwe, 2000a).

Regarding the large Te_8 entities, the (disordered) structure model in *Amm2* shows a lower energy than the corresponding (ordered) model in *A2* ($\Delta E = 0.16$ eV). The *Amm2* structure would imply the existence of bent Te_3 entities with bond angles of about $90.0 (1)^\circ$ in the planar Te layer, as mentioned before. Angular Te_3^{2-} anions are well known, e.g. from the binary dialkali metal tritellurides $A_2\text{Te}_3$ with $A = \text{K}, \text{Rb}$ or Cs (Eisenmann & Schäfer, 1978; Böttcher, 1980) and have Te–Te distances of about 2.80 Å, but significantly larger bond angles

of about 100° . These Te_3^{2-} anions are, however, more or less isolated in the structures and no interactions amongst them or with other anionic fragments are expected. Bent Te_3 entities with Te–Te–Te angles close to 90° were described as parts of the anionic substructure in disordered polytellurides like KRE_3Te_8 (Stöwe *et al.*, 2003; Patschke *et al.*, 1998) and $\text{RbUSb}_{0.33}\text{Te}_6$ (Choi & Kanatzidis, 2001), and in the modulated structures of $\text{K}_{1/3}\text{Ba}_{2/3}\text{AgTe}_2$ (Gourdon *et al.*, 2000), LnTe_3 (Malliakas *et al.*, 2005) and RESeTe_2 (Fokwa *et al.*, 2002; Fokwa Tsinde & Doert, 2005), for example.

Orthoslices of the ELI-D within the [Te] layers of the *Amm2* and the *P1* approximant are shown in Fig. 9. The isolines of both ELI-D images within the [Te] plane discriminates most of the observed Te atoms in three groups: isolated Te^{2-} , dinuclear Te_2^{2-} and bent trinuclear Te_3^{2-} anions. The ELI-D in the *P1* model suggest a slightly more pronounced tendency to form Te_2^{2-} dumbbells as main polynuclear building units, in accordance with the reported structures of rare earth metal sulfides and selenides (Doert & Müller, 2016) and with theoretical considerations for the rare earth metal selenides (Lee & Foran, 1994). As discussed above, these entities are expected to represent the dominant bonding interactions in the planar layer, but the local bonding situation and the stability of the corresponding fragment are also influenced by interactions with other telluride anions in the [Te] layers, as well as by the surrounding La atoms in the layers below and above. Indeed, substantial interactions between these small anionic fragments in the [Te] layer have to be considered based on relatively high isovalues of the ELI-D between the dominating species in all models (Fig. 9). For nonbonding or antibonding interactions, deep valleys (depicted in blue) would be expected, like, for example, the dark-blue regions between strongly localized lone-pair regions in *P1*.

The ELI-D slices in Fig. 9 show some additional interesting features. Significant localized lone-pair regions are found for those Te atoms located directly adjacent to vacancies. This may be taken as evidence for the anionic character of the [Te] layers. The respective lone pairs are localized in the structural voids with no hint of bonding interactions between Te fragments encasing the voids. The additional vacancies of the *P1*

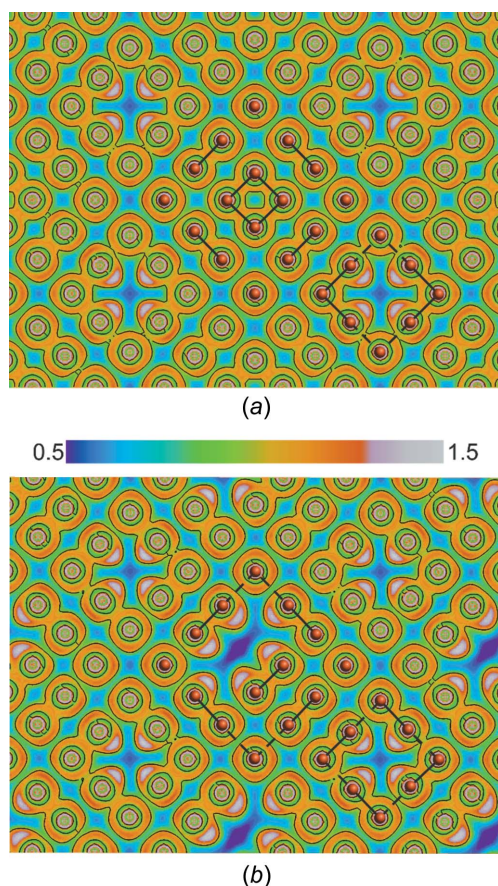


Figure 9 Orthoslices of ELI-D of the Te layer of $\text{LaTe}_{1.82(1)}$ with isocontour lines. (a) The largely unordered model in *Amm2*, with bent Te_3 units in the Te_8 entities and a Te_4 square. (b) The essentially ordered model in *P1*, exhibiting linear Te_2^{2-} units in the Te_8 entities and with only one Te_2^{2-} anion instead of a Te_4 square. Both pictures hint towards the interactions between different Te fragments in the planar layer.

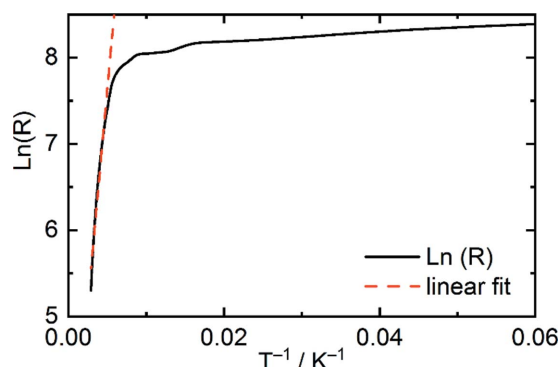


Figure 10 Temperature-dependent electrical resistance of $\text{LaTe}_{1.82(1)}$ between 7 and 345 K, showing a semiconducting behaviour.

model (Fig. 9b) seem to be used to accommodate the lone pairs of different anionic Te fragments, again supporting the ionic description of the [Te] layer and in accordance with the calculated band gap and the measured semiconducting properties of $\text{LaTe}_{1.81(2)}$ (see below).

Note, that the evaluated approximant structures indicate compositions of about $\text{LaTe}_{1.95}$ (*Amm2* and *A2*) and $\text{LaTe}_{1.875}$ (*P1*), *i.e.* a higher tellurium content as compared to the actual composition $\text{LaTe}_{1.82(1)}$. Thus, additional vacancies would be necessary to get a more realistic image of the Te substructure. The bonding features between different constituents should nevertheless be comparable.

3.7. Electrical resistance of $\text{LaTe}_{1.82(1)}$

The temperature-dependent electrical resistance of $\text{LaTe}_{1.82(1)}$ has been recorded by a four-point measurement between 7 and 345 K. The observed temperature dependence of the resistance of $\text{LaTe}_{1.82(1)}$ is characteristic for a semiconductor (Fig. 10). The band gap, E_g , can be estimated from the highest temperature ρ values using a fit of the form $\rho = \rho_0 \exp(E_g/2k_B T)$, where k_B is the Boltzmann constant and T is the absolute temperature. The estimated E_g value is 0.17 eV for $\text{LaTe}_{1.82(1)}$, which is slightly larger than the calculated value for the model in *A2* (*cf.* above). However, comparable compounds like $\text{NdTe}_{1.89(1)}$, $\text{GdTe}_{1.8}$ and $\text{SmTe}_{1.84}$ show similar band gaps of 0.14 (Stöwe, 2001), 0.19 (Poddig *et al.*, 2018) and 0.04 eV (Park *et al.*, 1998), respectively, in contrast to LaTe_2 , which was reported to be metallic (Stöwe, 2000a).

4. Conclusions

The modulated structure of the rare earth metal polytelluride $\text{LaTe}_{1.82(1)}$ has been solved and refined using the superspace approach. The diffraction pattern evidences that the tetragonal symmetry of the average structure is not preserved in the modulation. Two different models evaluated in superspace groups $Pmnm(\alpha, \beta, \frac{1}{2})000(-\alpha, \beta, \frac{1}{2})000$ (No. 59.2.51.39) and $Pm2_1n(\alpha, \beta, \frac{1}{2})000(-\alpha, \beta, \frac{1}{2})000$ (No. 31.2.51.35) show only slightly different results, suggesting that the highest possible superspace group $Pmnm(\alpha, \beta, \frac{1}{2})000(-\alpha, \beta, \frac{1}{2})000$ should describe the structure accordingly. In the regime of the different $REX_{2-\delta}$ compounds, $\text{LaTe}_{1.82(1)}$ may be best described as a depleted $REX_{1.9}$ or $REX_{1.875}$ structure. For the latter two structure types, it is possible to accommodate the respective anionic vacancies structurally isolated, *i.e.* separated between different (poly)telluride anions and in a commensurate superstructure. In the title compound, 18% of the Te_2 positions are unoccupied, which leads to two obvious consequences: a commensurate ordering of vacancies and remaining anions is not possible anymore, and a considerable number of adjacent anion defects occur. In other words, $\text{LaTe}_{1.82(1)}$ exhibits a higher propensity for missing Te_2^{2-} dianions. This description deviates significantly from the structures described for $RETe_{1.8}$ ($RE = \text{Sm, Gd-Dy}$; Ijjaali & Ibers, 2006; Wu *et al.*, 2002; Gulay *et al.*, 2007; Poddig *et al.*, 2018). However, this different structure fits well with the overall trend for the rare earth

metal tellurides $RETe_{2-\delta}$, where different structures have been observed for a similar composition, as pointed out for the stoichiometric $RETe_2$ ($RE = \text{La, Ce or Pr}$) compounds. Quantum mechanical calculations based on DFT with subsequent ELI-D-based bonding analysis for the ionic Te layer reveal Te_2^{2-} units as dominant species, however, with significant long-range interactions amongst them. Temperature-dependent resistance measurements suggest a semiconducting behaviour with a band gap of about 0.17 eV, which is in good agreement with comparable rare earth metal compounds.

Acknowledgements

KF acknowledges the Technische Universität Dresden for funding within the framework of a Maria Reiche fellowship.

Funding information

Funding for this research was provided by: Deutsche Forschungsgemeinschaft (grant No. Do 590/6 to TD).

References

- Assoud, A., Xu, J. & Kleinke, H. (2007). *Inorg. Chem.* **46**, 9906–9911.
- Barr, J., Gillespie, R. J., Kapoor, R. & Pez, G. P. (1968). *J. Am. Chem. Soc.* **90**, 6855–6856.
- Beck, J., Kasper, M. & Stankowski, A. (1997). *Chem. Ber.* **130**, 1189–1192.
- Becker, P. J. & Coppens, P. (1974). *Acta Cryst.* **A30**, 148–153.
- Blum, V., Gehrke, R., Hanke, F., Havu, P., Havu, V., Ren, X., Reuter, K. & Scheffler, M. (2009). *Comput. Phys. Commun.* **180**, 2175–2196.
- Böttcher, P. (1980). *J. Less-Common Met.* **70**, 263–271.
- Böttcher, P., Getzschmann, J. & Keller, R. (1993). *Z. Anorg. Allg. Chem.* **619**, 476–488.
- Brandenburg, K. (2019). *DIAMOND*. Crystal Impact GbR, Bonn, Germany.
- Bruker (2010). *APEX2*. Bruker AXS Inc., Madison, Wisconsin, USA.
- Bruker (2017). *SAINT-Plus*. Bruker AXS Inc., Madison, Wisconsin, USA.
- Choi, K.-S. & Kanatzidis, M. G. (2001). *J. Solid State Chem.* **161**, 17–22.
- Coelho, A. A. (2018). *J. Appl. Cryst.* **51**, 210–218.
- Dashjav, E., Doert, T., Böttcher, P., Mattausch, H. & Oeckler, O. (2000). *Z. Kristallogr. New Cryst. Struct.* **215**, 337–338.
- Doert, T., Dashjav, E. & Fokwa, B. P. T. (2007). *Z. Anorg. Allg. Chem.* **633**, 261–273.
- Doert, T., Graf, C., Lauxmann, P. & Schleid, T. (2007). *Z. Anorg. Allg. Chem.* **633**, 2719–2724.
- Doert, T., Graf, C., Schmidt, P., Vasilieva, I. G., Simon, P. & Carrillo-Cabrera, W. (2007). *J. Solid State Chem.* **180**, 496–509.
- Doert, T., Graf, C., Vasilyeva, I. G. & Schnelle, W. (2012). *Inorg. Chem.* **51**, 282–289.
- Doert, T. & Müller, C. J. (2016). *Binary Polysulfides and Polyselenides of Trivalent Rare-Earth Metals*, in *Reference Module in Chemistry, Molecular Sciences and Chemical Engineering*, edited by J. Reedijk. Waltham, MA: Elsevier.
- Dolomanov, O. V., Bourhis, L. J., Gildea, R. J., Howard, J. A. K. & Puschmann, H. (2009). *J. Appl. Cryst.* **42**, 339–341.
- Eisenmann, B. & Schäfer, H. (1978). *Angew. Chem.* **90**, 731.
- Fokwa, B. P. T., Doert, T., Simon, P., Söhnle, T. & Böttcher, P. (2002). *Z. Anorg. Allg. Chem.* **628**, 2612–2616.
- Fokwa Tsinde, B. P. & Doert, T. (2005). *Solid State Sci.* **7**, 573–587.
- Forge, F. & Beck, J. (2018). *Z. Anorg. Allg. Chem.* **644**, 1525–1531.
- Gourdon, O., Hanko, J., Boucher, F., Petricek, V., Whangbo, M.-H., Kanatzidis, M. G. & Evain, M. (2000). *Inorg. Chem.* **39**, 1398–1409.
- Graf, C. & Doert, T. (2009). *Z. Kristallogr. Cryst. Mater.* **224**, 568–579.

- Grupe, M. & Urland, W. (1991). *J. Less-Common Met.* **170**, 271–275.
- Gulay, L. D., Stępień-Damm, J., Daszkiewicz, M. & Pietraszko, A. (2007). *J. Alloys Compd.* **427**, 166–170.
- Ijjaali, I. & Ibers, J. A. (2006). *J. Solid State Chem.* **179**, 3456–3460.
- Klein Haneveld, A. & Jellinek, F. (1964). *Recl. Trav. Chim. Pays-Bas*, **83**, 776–783.
- Kohout, M. (2004). *Int. J. Quantum Chem.* **97**, 651–658.
- Kohout, M. (2006). *Faraday Discuss.* **135**, 43–54.
- Kohout, M. (2016). *DGrid*. Version 5.0. <http://www2.cfps.mpg.de/kohout/dgrid.html>.
- Krause, L., Herbst-Irmer, R., Sheldrick, G. M. & Stalke, D. (2015). *J. Appl. Cryst.* **48**, 3–10.
- Lee, S. & Foran, B. (1994). *J. Am. Chem. Soc.* **116**, 154–161.
- Lee, A. van der, Hoistad, L. M., Evain, M., Foran, B. J. & Lee, S. (1997). *Chem. Mater.* **9**, 218–226.
- Malliakas, C., Billinge, S. J. L., Kim, H. J. & Kanatzidis, M. G. (2005). *J. Am. Chem. Soc.* **127**, 6510–6511.
- Müller, C. J., Schwarz, U. & Doert, T. (2012). *Z. Anorg. Allg. Chem.* **638**, 2477–2484.
- Onken, H., Vierheilig, K. & Hahn, H. (1964). *Z. Anorg. Allg. Chem.* **333**, 267–279.
- Palatinus, L. & Chapuis, G. (2007). *J. Appl. Cryst.* **40**, 786–790.
- Park, S.-M., Park, S.-J. & Kim, S.-J. (1998). *J. Solid State Chem.* **140**, 300–306.
- Patschke, R., Heising, J., Schindler, J., Kannewurf, C. R. & Kanatzidis, M. (1998). *J. Solid State Chem.* **135**, 111–115.
- Pendás, A. M., Kohout, M., Blanco, M. A. & Francisco, E. (2012). *Modern Charge-Density Analysis*, pp. 303–358. Dordrecht, Heidelberg, London, New York: Springer.
- Perdew, J. P., Burke, K. & Ernzerhof, M. (1996). *Phys. Rev. Lett.* **77**, 3865–3868.
- Petříček, V., Dušek, M. & Palatinus, L. (2014). *Z. Kristallogr. Cryst. Mater.* **229**, 345–352.
- Petříček, V., Eigner, V., Dušek, M. & Čejchan, A. (2016). *Z. Kristallogr. Cryst. Mater.* **231**, 301–312.
- Plambeck-Fischer, P., Abriel, W. & Urland, W. (1989). *J. Solid State Chem.* **78**, 164–169.
- Poddig, H., Donath, T., Gebauer, P., Finzel, K., Kohout, M., Wu, Y., Schmidt, P. & Doert, T. (2018). *Z. Anorg. Allg. Chem.* **644**, 1886–1896.
- Rothman, M. J., Bartell, L. S., Ewig, C. S. & Wazer, J. R. V. (1980). *J. Comput. Chem.* **1**, 64–68.
- Ruck, M. & Locherer, F. (2015). *Coord. Chem. Rev.* **285**, 1–10.
- Rundle, R. E. (1963). *J. Am. Chem. Soc.* **85**, 112–113.
- Sheldrick, G. M. (2015a). *Acta Cryst.* **A71**, 3–8.
- Sheldrick, G. M. (2015b). *Acta Cryst.* **C71**, 3–8.
- Stokes, H. T., Campbell, B. J. & van Smaalen, S. (2011). *Acta Cryst.* **A67**, 45–55.
- Stöwe, K. (2000a). *J. Solid State Chem.* **149**, 155–166.
- Stöwe, K. (2000b). *J. Alloys Compd.* **307**, 101–110.
- Stöwe, K. (2000c). *Z. Anorg. Allg. Chem.* **626**, 803–811.
- Stöwe, K. (2001). *Z. Kristallogr. Cryst. Mater.* **216**, 215–224.
- Stöwe, K., Napoli, C. & Appel, S. (2003). *Z. Anorg. Allg. Chem.* **629**, 1925–1928.
- Tamazyan, R., Arnold, H., Molchanov, V., Kuzmicheva, G. & Vasileva, I. (2000). *Z. Kristallogr. Cryst. Mater.* **215**, 272–277.
- Urland, W., Plambeck-Fischer, P. & Grupe, M. (1989). *Z. Naturforsch. Teil B*, **44**, 261–264.
- Wu, Y., Doert, T. & Böttcher, P. (2002). *Z. Anorg. Allg. Chem.* **628**, 2216.

supporting information

Acta Cryst. (2020). C76, 530-540 [https://doi.org/10.1107/S2053229620005094]

LaTe_{1.82(1)}: modulated crystal structure and chemical bonding of a chalcogen-deficient rare earth metal polytelluride

Hagen Poddig, Kati Finzel and Thomas Doert

Computing details

For both structures, data collection: *APEX2* (Bruker, 2010). Cell refinement: *APEX2* (Bruker, 2010) for (I); *SAINT-Plus* (Bruker, 2017) for (II). For both structures, data reduction: *SAINT-Plus* (Bruker, 2017). Program(s) used to solve structure: *SHELXT2014* (Sheldrick, 2015a) for (I); *SUPERFLIP* (Palatinus & Chapuis, 2007) for (II). Program(s) used to refine structure: *SHELXL2019* (Sheldrick, 2015b) for (I); *JANA2006* (Petricek *et al.*, 2014) for (II). For both structures, molecular graphics: *OLEX2* (Dolomanov *et al.*, 2009) and *DIAMOND* (Brandenburg, 2019). Software used to prepare material for publication: *OLEX2* (Dolomanov *et al.*, 2009) for (I); *JANA2006* (Petricek *et al.*, 2014) for (II).

Lanthanum telluride (1/1.8) (I)

Crystal data

LaTe _{1.81}	$D_x = 6.621 \text{ Mg m}^{-3}$
$M_r = 370.50$	Mo $K\alpha$ radiation, $\lambda = 0.71073 \text{ \AA}$
Tetragonal, $P4/nmm:1$	Cell parameters from 872 reflections
$a = 4.4996 (5) \text{ \AA}$	$\theta = 4.4\text{--}34.7^\circ$
$c = 9.1794 (12) \text{ \AA}$	$\mu = 25.18 \text{ mm}^{-1}$
$V = 185.85 (3) \text{ \AA}^3$	$T = 296 \text{ K}$
$Z = 2$	Block, metallic black
$F(000) = 303$	$0.03 \times 0.02 \times 0.02 \text{ mm}$

Data collection

Bruker APEXII CCD diffractometer	351 independent reflections
Radiation source: sealed X-ray tube profile data from CCD detector scans	289 reflections with $I > 2\sigma(I)$
Absorption correction: multi-scan (SADABS; Krause <i>et al.</i> , 2015)	$R_{\text{int}} = 0.046$
$T_{\text{min}} = 0.641$, $T_{\text{max}} = 0.748$	$\theta_{\text{max}} = 38.5^\circ$, $\theta_{\text{min}} = 2.2^\circ$
3402 measured reflections	$h = -7 \rightarrow 7$
	$k = -7 \rightarrow 7$
	$l = -8 \rightarrow 15$

Refinement

Refinement on F^2	Secondary atom site location: difference Fourier map
Least-squares matrix: full	$w = 1/[\sigma^2(F_o^2) + (0.0248P)^2 + 0.9467P]$
$R[F^2 > 2\sigma(F^2)] = 0.024$	where $P = (F_o^2 + 2F_c^2)/3$
$wR(F^2) = 0.057$	$(\Delta/\sigma)_{\text{max}} < 0.001$
$S = 1.07$	$\Delta\rho_{\text{max}} = 3.15 \text{ e \AA}^{-3}$
351 reflections	$\Delta\rho_{\text{min}} = -2.35 \text{ e \AA}^{-3}$
11 parameters	
0 restraints	
Primary atom site location: dual	

Extinction correction: SHELXL2019
(Sheldrick, 2015b),
 $F_c^* = kF_c [1 + 0.001x F_c^2 \lambda^3 / \sin(2\theta)]^{-1/4}$

Extinction coefficient: 0.0266 (18)
Absolute structure: No quotients, so Flack
parameter determined by classical intensity fit

Special details

Geometry. All esds (except the esd in the dihedral angle between two l.s. planes) are estimated using the full covariance matrix. The cell esds are taken into account individually in the estimation of esds in distances, angles and torsion angles; correlations between esds in cell parameters are only used when they are defined by crystal symmetry. An approximate (isotropic) treatment of cell esds is used for estimating esds involving l.s. planes.

Refinement. Single-crystal X-ray diffraction was performed with the four-circle diffractometer Kappa Apex2 (Bruker) equipped with a CCD-detector using graphite-monochromated Mo-K α radiation ($\lambda = 0.71073$ Å) at 296 (1) K. Data for the average structure was corrected for Lorentz and polarization factors, and multi-scan absorption corrections was applied (Krause *et al.*, 2015). The structure was solved using the dual space approach of the program package *SHELXT* (Sheldrick, 2015a). Structure refinement was performed with the program package *SHELXL* against F^2 including anisotropic displacement parameters for all atoms (Sheldrick, 2015b).

Krause, L., Herbst-Irmer, R., Sheldrick, G. M. & Stalke, D. (2015). *J. Appl. Cryst.* **48**, 3–10.

Sheldrick, G. M. (2015a). *Acta Cryst.* **A71**, 3–8.

Sheldrick, G. M. (2015b). *Acta Cryst.* **C71**, 3–8.

Fractional atomic coordinates and isotropic or equivalent isotropic displacement parameters (Å²)

	x	y	z	U_{iso}^*/U_{eq}	Occ. (<1)
La1	0.000000	0.500000	0.27121 (7)	0.01498 (15)	
Te1	0.000000	0.500000	0.63329 (7)	0.01164 (15)	
Te2	0.000000	0.000000	0.000000	0.0408 (4)	0.813 (4)

Atomic displacement parameters (Å²)

	U^{11}	U^{22}	U^{33}	U^{12}	U^{13}	U^{23}
La1	0.00971 (16)	0.00971 (16)	0.0255 (3)	0.000	0.000	0.000
Te1	0.00909 (17)	0.00909 (17)	0.0167 (3)	0.000	0.000	0.000
Te2	0.0568 (6)	0.0568 (6)	0.0088 (4)	0.000	0.000	0.000

Geometric parameters (Å, °)

La1—Te1 ⁱ	3.3002 (3)	La1—Te2 ^{vi}	3.3555 (6)
La1—Te1 ⁱⁱ	3.3002 (3)	La1—Te2 ^{vii}	3.3555 (5)
La1—Te1 ⁱⁱⁱ	3.3002 (3)	Te2—Te2 ^{vi}	3.1817 (2)
La1—Te1 ^{iv}	3.3002 (3)	Te2—Te2 ^{viii}	3.1817 (2)
La1—Te1	3.3237 (10)	Te2—Te2 ^v	3.1817 (2)
La1—Te2 ^v	3.3555 (6)	Te2—Te2 ^{ix}	3.1817 (2)
La1—Te2	3.3555 (5)		
Te1 ⁱ —La1—Te1 ⁱⁱ	149.19 (3)	La1 ⁱ —Te1—La1 ⁱⁱⁱ	85.954 (10)
Te1 ⁱ —La1—Te1 ⁱⁱⁱ	85.954 (10)	La1 ⁱⁱ —Te1—La1 ⁱⁱⁱ	85.954 (9)
Te1 ⁱⁱ —La1—Te1 ⁱⁱⁱ	85.954 (10)	La1 ⁱ —Te1—La1 ^{iv}	85.954 (9)
Te1 ⁱ —La1—Te1 ^{iv}	85.954 (9)	La1 ⁱⁱ —Te1—La1 ^{iv}	85.954 (10)
Te1 ⁱⁱ —La1—Te1 ^{iv}	85.954 (10)	La1 ⁱⁱⁱ —Te1—La1 ^{iv}	149.19 (3)
Te1 ⁱⁱⁱ —La1—Te1 ^{iv}	149.19 (3)	La1 ⁱ —Te1—La1	105.404 (15)
Te1 ⁱ —La1—Te1	74.597 (15)	La1 ⁱⁱ —Te1—La1	105.403 (15)

Te1 ⁱⁱ —La1—Te1	74.597 (15)	La1 ⁱⁱⁱ —Te1—La1	105.404 (15)
Te1 ⁱⁱⁱ —La1—Te1	74.597 (15)	La1 ^{iv} —Te1—La1	105.404 (15)
Te1 ^{iv} —La1—Te1	74.597 (15)	Te2 ^{vi} —Te2—Te2 ^{viii}	180.0
Te1 ⁱ —La1—Te2 ^v	130.854 (14)	Te2 ^{vi} —Te2—Te2 ^v	90.000 (6)
Te1 ⁱⁱ —La1—Te2 ^v	74.930 (12)	Te2 ^{viii} —Te2—Te2 ^v	90.000 (6)
Te1 ⁱⁱⁱ —La1—Te2 ^v	74.930 (12)	Te2 ^{vi} —Te2—Te2 ^{ix}	90.000 (6)
Te1 ^{iv} —La1—Te2 ^v	130.854 (14)	Te2 ^{viii} —Te2—Te2 ^{ix}	90.000 (6)
Te1—La1—Te2 ^v	137.896 (9)	Te2 ^v —Te2—Te2 ^{ix}	180.0
Te1 ⁱ —La1—Te2	130.854 (14)	Te2 ^{vi} —Te2—La1 ^v	118.301 (6)
Te1 ⁱⁱ —La1—Te2	74.930 (11)	Te2 ^{viii} —Te2—La1 ^v	61.699 (6)
Te1 ⁱⁱⁱ —La1—Te2	130.854 (14)	Te2 ^v —Te2—La1 ^v	61.699 (6)
Te1 ^{iv} —La1—Te2	74.930 (11)	Te2 ^{ix} —Te2—La1 ^v	118.301 (6)
Te1—La1—Te2	137.896 (8)	Te2 ^{vi} —Te2—La1 ^x	118.301 (5)
Te2 ^v —La1—Te2	56.601 (10)	Te2 ^{viii} —Te2—La1 ^x	61.699 (5)
Te1 ⁱ —La1—Te2 ^{vi}	74.930 (12)	Te2 ^v —Te2—La1 ^x	118.301 (5)
Te1 ⁱⁱ —La1—Te2 ^{vi}	130.854 (14)	Te2 ^{ix} —Te2—La1 ^x	61.699 (5)
Te1 ⁱⁱⁱ —La1—Te2 ^{vi}	130.854 (14)	La1 ^v —Te2—La1 ^x	123.398 (10)
Te1 ^{iv} —La1—Te2 ^{vi}	74.930 (12)	Te2 ^{vi} —Te2—La1 ^{vi}	61.699 (6)
Te1—La1—Te2 ^{vi}	137.896 (9)	Te2 ^{viii} —Te2—La1 ^{vi}	118.301 (6)
Te2 ^v —La1—Te2 ^{vi}	84.208 (18)	Te2 ^v —Te2—La1 ^{vi}	118.301 (6)
Te2—La1—Te2 ^{vi}	56.601 (10)	Te2 ^{ix} —Te2—La1 ^{vi}	61.699 (6)
Te1 ⁱ —La1—Te2 ^{vii}	74.930 (11)	La1 ^v —Te2—La1 ^{vi}	84.208 (17)
Te1 ⁱⁱ —La1—Te2 ^{vii}	130.854 (14)	La1 ^x —Te2—La1 ^{vi}	123.398 (10)
Te1 ⁱⁱⁱ —La1—Te2 ^{vii}	74.930 (11)	Te2 ^{vi} —Te2—La1	61.699 (5)
Te1 ^{iv} —La1—Te2 ^{vii}	130.854 (14)	Te2 ^{viii} —Te2—La1	118.301 (5)
Te1—La1—Te2 ^{vii}	137.896 (8)	Te2 ^v —Te2—La1	61.699 (5)
Te2 ^v —La1—Te2 ^{vii}	56.601 (10)	Te2 ^{ix} —Te2—La1	118.301 (5)
Te2—La1—Te2 ^{vii}	84.208 (16)	La1 ^v —Te2—La1	123.399 (10)
Te2 ^{vi} —La1—Te2 ^{vii}	56.601 (10)	La1 ^x —Te2—La1	84.208 (16)
La1 ⁱ —Te1—La1 ⁱⁱ	149.19 (3)	La1 ^{vi} —Te2—La1	123.398 (10)

Symmetry codes: (i) $-x+1/2, -y+3/2, -z+1$; (ii) $-x-1/2, -y+1/2, -z+1$; (iii) $-x-1/2, -y+3/2, -z+1$; (iv) $-x+1/2, -y+1/2, -z+1$; (v) $-x-1/2, -y+1/2, -z$; (vi) $-x+1/2, -y+1/2, -z$; (vii) $x, y+1, z$; (viii) $-x-1/2, -y-1/2, -z$; (ix) $-x+1/2, -y-1/2, -z$; (x) $x, y-1, z$.

(II)

Crystal data

LaTe_{1.811(4)}

$M_r = 370$

Orthorhombic, $Pmnm\uparrow$

$\mathbf{q}_1 = 0.275080\mathbf{a}^* + 0.309805\mathbf{b}^* + 0.500000\mathbf{c}^*$;

$\mathbf{q}_2 = -0.275080\mathbf{a}^* + 0.309805\mathbf{b}^* + 0.500000\mathbf{c}^*$

$a = 4.4861$ (5) Å

$b = 4.5030$ (5) Å

$c = 9.1806$ (11) Å

$V = 185.46$ (4) Å³

$Z = 2$

$F(000) = 303$

$D_x = 6.626$ Mg m⁻³

Mo $K\alpha$ radiation, $\lambda = 0.71073$ Å

Cell parameters from 872 reflections

$\theta = 4.4\text{--}34.7^\circ$

$\mu = 25.20$ mm⁻¹

$T = 296$ K

Block, black

$0.06 \times 0.05 \times 0.01$ mm

† Symmetry operations: (1) x_1, x_2, x_3, x_4, x_5 ; (2) $-x_1, -x_2, x_3, x_3-x_4, x_3-x_5$; (3) $-x_1+1/2, x_2+1/2, -x_3, -x_3+x_5, -x_3+x_4$; (4) $x_1+1/2, -x_2+1/2, -x_3, -x_5, -x_4$; (5) $-x_1+1/2, -x_2+1/2, -x_3, -x_4, -x_5$; (6) $x_1+1/2, x_2+1/2, -x_3, -x_3+x_4, -x_3+x_5$; (7) $x_1, -x_2, x_3, x_3-x_5, x_3-x_4$; (8) $-x_1, x_2, x_3, x_5, x_4$.

Data collection

Bruker APEXII CCD diffractometer	1757 independent reflections
Radiation source: sealed X-ray tube	738 reflections with $I > 3\sigma(I)$
profile data from CCD detector scans	$R_{\text{int}} = 0.156$
Absorption correction: gaussian	$\theta_{\text{max}} = 38.4^\circ, \theta_{\text{min}} = 2.2^\circ$
Jana2006	$h = -7 \rightarrow 8$
$T_{\text{min}} = 0.393, T_{\text{max}} = 0.498$	$k = -8 \rightarrow 8$
30619 measured reflections	$l = -16 \rightarrow 9$

Refinement

Refinement on F^2	Weighting scheme based on measured s.u.'s $w = 1/(\sigma^2(I) + 0.0004I^2)$
$R[F > 3\sigma(F)] = 0.050$	$(\Delta/\sigma)_{\text{max}} = 0.045$
$wR(F) = 0.111$	$\Delta\rho_{\text{max}} = 15.11 \text{ e } \text{\AA}^{-3}$
$S = 1.26$	$\Delta\rho_{\text{min}} = -17.25 \text{ e } \text{\AA}^{-3}$
1757 reflections	Extinction correction: B-C type 1 Gaussian
24 parameters	isotropic (Becker & Coppens, 1974)
0 restraints	Extinction coefficient: 1500 (80)
1 constraint	

Fractional atomic coordinates and isotropic or equivalent isotropic displacement parameters (\AA^2)

	x	y	z	$U_{\text{iso}}^*/U_{\text{eq}}$	Occ. (<1)
La1	0	0.5	0.27147 (8)	0.01052 (18)	
Te1	0	0.5	0.63322 (8)	0.01043 (19)	
Te2	0	0	0	0.0204 (4)	0.811 (4)

Atomic displacement parameters (\AA^2)

	U^{11}	U^{22}	U^{33}	U^{12}	U^{13}	U^{23}
La1	0.0099 (3)	0.0090 (3)	0.0127 (4)	0	0	0
Te1	0.0096 (3)	0.0095 (3)	0.0121 (4)	0	0	0
Te2	0.0258 (7)	0.0266 (8)	0.0088 (5)	0	0	0

Geometric parameters ($\text{\AA}, ^\circ$)

	Average	Minimum	Maximum
La1—Te1	3.319 (2)	3.234 (2)	3.408 (2)
La1—Te1 ⁱ	3.296 (3)	3.245 (3)	3.353 (3)
La1—Te1 ⁱⁱ	3.297 (3)	3.245 (3)	3.354 (3)
La1—Te1 ⁱⁱⁱ	3.296 (3)	3.245 (3)	3.353 (3)
La1—Te1 ^{iv}	3.297 (3)	3.245 (3)	3.354 (3)
La1—Te2	3.371 (2)	3.253 (3)	3.475 (3)
La1—Te2 ^v	3.363 (2)	3.253 (3)	3.475 (3)
La1—Te2 ^{vi}	3.361 (3)	3.248 (4)	3.463 (4)

La1—Te2 ^{vii}	3.361 (3)	3.248 (4)	3.463 (4)
Te2—Te2 ^{viii}	3.167 (3)	2.799 (5)	3.558 (5)
Te2—Te2 ^{vi}	3.167 (3)	2.799 (5)	3.558 (5)
Te2—Te2 ^{ix}	3.167 (3)	2.799 (5)	3.558 (5)
Te2—Te2 ^{vii}	3.167 (3)	2.799 (5)	3.558 (5)
Te1—La1—Te1 ⁱ	74.66 (5)	71.62 (5)	77.67 (5)
Te1—La1—Te1 ⁱⁱ	74.73 (5)	71.63 (5)	77.66 (5)
Te1—La1—Te1 ⁱⁱⁱ	74.66 (5)	71.62 (5)	77.67 (5)
Te1—La1—Te1 ^{iv}	74.73 (5)	71.63 (5)	77.66 (5)
Te1—La1—Te2	138.00 (7)	131.71 (7)	144.29 (8)
Te1—La1—Te2 ^v	138.09 (7)	131.70 (7)	144.25 (8)
Te1—La1—Te2 ^{vi}	138.12 (7)	132.30 (6)	143.81 (7)
Te1—La1—Te2 ^{vii}	138.12 (7)	132.30 (6)	143.81 (7)
Te1 ⁱ —La1—Te1 ⁱⁱ	86.19 (5)	84.52 (5)	87.67 (5)
Te1 ⁱ —La1—Te1 ⁱⁱⁱ	85.78 (5)	84.22 (5)	87.09 (5)
Te1 ⁱ —La1—Te1 ^{iv}	149.39 (6)	143.50 (6)	155.11 (7)
Te1 ⁱ —La1—Te2	74.94 (7)	72.45 (7)	77.30 (7)
Te1 ⁱ —La1—Te2 ^v	130.63 (8)	125.30 (8)	136.53 (8)
Te1 ⁱ —La1—Te2 ^{vi}	75.07 (7)	72.70 (7)	77.50 (7)
Te1 ⁱ —La1—Te2 ^{vii}	130.42 (8)	125.13 (8)	136.45 (8)
Te1 ⁱⁱ —La1—Te1 ⁱⁱⁱ	149.39 (6)	143.50 (6)	155.11 (7)
Te1 ⁱⁱ —La1—Te1 ^{iv}	85.78 (5)	84.22 (5)	87.08 (5)
Te1 ⁱⁱ —La1—Te2	130.63 (8)	125.33 (8)	136.51 (8)
Te1 ⁱⁱ —La1—Te2 ^v	74.95 (7)	72.45 (7)	77.29 (7)
Te1 ⁱⁱ —La1—Te2 ^{vi}	75.16 (7)	72.70 (7)	77.51 (7)
Te1 ⁱⁱ —La1—Te2 ^{vii}	130.54 (8)	125.09 (8)	136.47 (8)
Te1 ⁱⁱⁱ —La1—Te1 ^{iv}	86.19 (5)	84.52 (5)	87.67 (5)
Te1 ⁱⁱⁱ —La1—Te2	74.94 (7)	72.45 (7)	77.30 (7)
Te1 ⁱⁱⁱ —La1—Te2 ^v	130.63 (8)	125.30 (8)	136.53 (8)
Te1 ⁱⁱⁱ —La1—Te2 ^{vi}	130.42 (8)	125.13 (8)	136.45 (8)
Te1 ⁱⁱⁱ —La1—Te2 ^{vii}	75.07 (7)	72.70 (7)	77.50 (7)
Te1 ^{iv} —La1—Te2	130.63 (8)	125.33 (8)	136.51 (8)
Te1 ^{iv} —La1—Te2 ^v	74.95 (7)	72.45 (7)	77.29 (7)
Te1 ^{iv} —La1—Te2 ^{vi}	130.54 (8)	125.09 (8)	136.47 (8)
Te1 ^{iv} —La1—Te2 ^{vii}	75.16 (7)	72.70 (7)	77.51 (7)
Te2—La1—Te2 ^v	83.88 (7)	71.67 (7)	96.54 (6)
Te2—La1—Te2 ^{vi}	56.18 (7)	48.42 (7)	64.86 (7)
Te2—La1—Te2 ^{vii}	56.18 (7)	48.42 (7)	64.86 (7)
Te2 ^v —La1—Te2 ^{vi}	56.28 (7)	48.45 (7)	64.83 (7)
Te2 ^v —La1—Te2 ^{vii}	56.28 (7)	48.45 (7)	64.83 (7)
Te2 ^{vi} —La1—Te2 ^{vii}	83.69 (6)	72.62 (6)	95.33 (6)
La1—Te1—La1 ⁱ	105.41 (6)	102.47 (5)	108.25 (5)
La1—Te1—La1 ⁱⁱ	105.30 (6)	102.48 (5)	108.24 (5)
La1—Te1—La1 ⁱⁱⁱ	105.41 (6)	102.47 (5)	108.25 (5)
La1—Te1—La1 ^{iv}	105.30 (6)	102.48 (5)	108.24 (5)
La1 ⁱ —Te1—La1 ⁱⁱ	86.21 (5)	85.55 (5)	86.71 (5)
La1 ⁱ —Te1—La1 ⁱⁱⁱ	85.79 (5)	85.18 (5)	86.27 (5)

La1 ⁱ —Te1—La1 ^{iv}	149.29 (6)	144.20 (7)	154.25 (7)
La1 ⁱⁱ —Te1—La1 ⁱⁱⁱ	149.29 (6)	144.20 (7)	154.25 (7)
La1 ⁱⁱ —Te1—La1 ^{iv}	85.80 (5)	85.18 (5)	86.27 (5)
La1 ⁱⁱⁱ —Te1—La1 ^{iv}	86.21 (5)	85.55 (5)	86.71 (5)
La1 ^x —Te2—La1	83.87 (5)	80.45 (7)	88.10 (7)
La1 ^x —Te2—La1 ^{viii}	123.37 (7)	114.57 (9)	132.12 (6)
La1 ^x —Te2—La1 ^{ix}	123.37 (7)	114.57 (9)	132.12 (6)
La1 ^x —Te2—Te2 ^{viii}	61.76 (6)	57.09 (5)	66.19 (6)
La1 ^x —Te2—Te2 ^{vi}	118.22 (7)	113.84 (6)	122.96 (7)
La1 ^x —Te2—Te2 ^{ix}	61.76 (6)	57.09 (5)	66.19 (6)
La1 ^x —Te2—Te2 ^{vii}	118.22 (7)	113.84 (6)	122.96 (7)
La1—Te2—La1 ^{viii}	123.37 (7)	114.57 (9)	132.12 (6)
La1—Te2—La1 ^{ix}	123.37 (7)	114.57 (9)	132.12 (6)
La1—Te2—Te2 ^{viii}	118.22 (7)	113.84 (6)	122.96 (7)
La1—Te2—Te2 ^{vi}	61.76 (6)	57.09 (5)	66.19 (6)
La1—Te2—Te2 ^{ix}	118.22 (7)	113.84 (6)	122.96 (7)
La1—Te2—Te2 ^{vii}	61.76 (6)	57.09 (5)	66.19 (6)
La1 ^{viii} —Te2—La1 ^{ix}	83.64 (5)	79.93 (7)	88.22 (7)
La1 ^{viii} —Te2—Te2 ^{viii}	61.92 (6)	57.32 (6)	66.24 (7)
La1 ^{viii} —Te2—Te2 ^{vi}	61.92 (6)	57.32 (6)	66.24 (7)
La1 ^{viii} —Te2—Te2 ^{ix}	118.09 (7)	113.58 (9)	122.75 (8)
La1 ^{viii} —Te2—Te2 ^{vii}	118.09 (7)	113.58 (9)	122.75 (8)
La1 ^{ix} —Te2—Te2 ^{viii}	118.09 (7)	113.58 (9)	122.75 (8)
La1 ^{ix} —Te2—Te2 ^{vi}	118.09 (7)	113.58 (9)	122.75 (8)
La1 ^{ix} —Te2—Te2 ^{ix}	61.92 (6)	57.32 (6)	66.24 (7)
La1 ^{ix} —Te2—Te2 ^{vii}	61.92 (6)	57.32 (6)	66.24 (7)
Te2 ^{viii} —Te2—Te2 ^{vi}	90.14 (9)	88.89 (9)	91.31 (7)
Te2 ^{viii} —Te2—Te2 ^{ix}	89.86 (9)	88.67 (7)	91.14 (8)
Te2 ^{viii} —Te2—Te2 ^{vii}	179.76 (9)	179.54 (9)	180
Te2 ^{vi} —Te2—Te2 ^{ix}	179.76 (9)	179.54 (9)	180
Te2 ^{vi} —Te2—Te2 ^{vii}	89.86 (9)	88.67 (7)	91.14 (8)
Te2 ^{ix} —Te2—Te2 ^{vii}	90.14 (9)	88.89 (9)	91.31 (7)

Symmetry codes: (i) $-x_1-1/2, x_2-1/2, -x_3+1, -x_3+x_5, -x_3+x_4$; (ii) $-x_1-1/2, x_2+1/2, -x_3+1, -x_3+x_5, -x_3+x_4$; (iii) $-x_1+1/2, x_2-1/2, -x_3+1, -x_3+x_5, -x_3+x_4$; (iv) $-x_1+1/2, x_2+1/2, -x_3+1, -x_3+x_5, -x_3+x_4$; (v) $x_1, x_2+1, x_3, x_4, x_5$; (vi) $-x_1-1/2, x_2+1/2, -x_3, -x_3+x_5, -x_3+x_4$; (vii) $-x_1+1/2, x_2+1/2, -x_3, -x_3+x_5, -x_3+x_4$; (viii) $-x_1-1/2, x_2-1/2, -x_3, -x_3+x_5, -x_3+x_4$; (ix) $-x_1+1/2, x_2-1/2, -x_3, -x_3+x_5, -x_3+x_4$; (x) $x_1, x_2-1, x_3, x_4, x_5$.